

GPU-Accelerated Analytic Simulation of Sparse Signals in Pixelated Time Projection Detector

YouSEN Zhang, Brett VIREN, Mary BISHAI, Sergey MARTYNEKO, Xin QIAN, Rado RAZAKAMIANDRA, Brooke RUSSELL

Abstract—This paper presents a GPU-accelerated simulation package, TRED, for next-generation neutrino detectors with pixelated charge readout, leveraging community-driven software ecosystems to ensure sustainability and extensibility. We introduce two generic contributions: (i) an effective-charge calculation based on Gaussian quadrature rules for numerical integration, and (ii) a sparse, block-binned tensor representation that enables efficient FFT-based computation of induced signals on readout electrodes for sparsely activated detector volumes. The former captures sub-grid structure without requiring dense sampling, while the latter achieves low memory usage and scalable runtime, as demonstrated in benchmark studies. The underlying data representation is applicable to large-scale detectors and to other computational problems involving sparse activity.

Index Terms—Elementary particles, Hardware acceleration, Parallel processing

I. INTRODUCTION

THE Deep Underground Neutrino Experiment (DUNE) designs, constructs, and operates both the near-detector complex at Fermilab and the far detector systems at the Sanford Underground Research Facility, located approximately 1,300 km downstream [1], [2]. One component of the DUNE near-detector complex is a liquid-argon time-projection chamber (ND-LAr), which employs the same target nucleus and detector technology as the far detector to reduce detector-related systematic uncertainties [2]. LArTPCs are fully active, homogeneous detectors that record millimeter-scale tomographic images of ionization charge together with prompt scintillation light, enabling precise three-dimensional event reconstruction. Owing to the high-power, wide-band neutrino beam provided by the Long-Baseline Neutrino Facility, initially operating at 1.2 MW and upgradable to 2.4 MW, the near site experiences $\mathcal{O}(10^2)$ neutrino–argon interactions per beam spill. This high interaction rate results in dense, highly overlapping activity and imposes stringent requirements on detector readout, motivating a modular LArTPC design with pixelated charge readout capable of resolving localized charge deposits.

This work was supported in part by the U.S. Department of Energy (DOE), Office of Science, Office of High Energy Physics, under Contract No. DE-SC0012704. (*Corresponding author: YouSEN Zhang*).

YouSEN Zhang, Brett VIREN, Mary BISHAI, Sergey MARTYNEKO, and Xin QIAN are with the Physics Department, Brookhaven National Laboratory, Upton, NY 11973 USA (e-mail: yzhang11@bnl.gov).

Xin QIAN is also with the Department of Physics and Astronomy, Stony Brook University, Stony Brook, NY 11794 USA.

Rado RAZAKAMIANDRA is with the Department of Physics and Astronomy, Stony Brook University, Stony Brook, NY 11794 USA.

Brooke RUSSELL is with the Department of Physics, Massachusetts Institute of Technology, Cambridge, MA 02139 USA.

The ND-LAr detector comprises an active volume of approximately $7 \times 5 \times 3 \text{ m}^3$ distributed across 35 TPC modules with millimeter-scale spatial sampling, resulting in $\mathcal{O}(5 \times 10^5)$ readout channels per module. Traditional CPU-based C++ frameworks face significant challenges in scaling to the large channel counts characteristic of ND-LAr data, and GPU-based approaches have emerged as a viable and necessary direction. Recent pioneering work has demonstrated the feasibility of highly parallelized GPU simulations for pixelated LArTPCs [3]. However, such approaches can still place substantial demands on GPU memory and hardware capabilities. Efficiently processing highly sparse detector data remains a challenge for GPU architectures, which are typically optimized for dense, regular workloads. These considerations motivated the design developed in this work. It focuses on scalability to the available GPU resources, exploits the sparseness of localized activity to efficiently process data for large detector volumes while retaining high-fidelity.

In this work, we present a GPU-native simulation package, TRED, built on community-driven software ecosystems, exemplified by PyTorch [4], to ensure long-term sustainability and extensibility, and tailored to the highly sparse and localized data characteristic of LArTPC detectors. We introduce a high-fidelity effective-charge representation of the ionization distribution after recombination and transport, together with a block-sparse binned tensor data structure that preserves locality while enabling efficient batched execution on GPUs. The induced signal on electrodes admits an analytic expression as a convolution of the effective-charge distribution with the detector Green’s function. The block-sparse binned representation enables this convolution to be evaluated using FFT-based methods on sparse charge distributions, without constructing a global dense grid.

Although developed with the DUNE ND-LAr detector in mind, the underlying concepts are applicable to a wider class of large-volume detectors with sparse activity, including the simulation of ionization charge signals in projective-readout LArTPCs such as the DUNE far detector. The block-based sparse data representation further supports broader applicability, including sparse sub-manifold convolution networks [5] used in machine learning.

Section II discusses the simulated detector physics in LArTPCs. Section III describes the software design and implementation of TRED. Section IV presents performance measurements, resource scaling, and associated limitations. Section V discusses these results in a broader physics and computing context. We summarize our results and outline future directions in Sec. VI.

II. SIMULATION FRAMEWORK AND SIGNAL FORMATION

A. Detector physics and simulation workflow

In a LArTPC, charged particles traversing the detector deposit energy in the argon medium, producing ionization electrons and scintillation light. A fraction of the ionization electrons recombines with argon ions, while the remaining free electrons drift toward the anode under an externally applied electric field and induce signals on the readout electrodes. During transport, drifting electrons may be attenuated by attachment to electronegative impurities and they may undergo spatial diffusion. These effects are accounted for in the simulation through parameterized models of recombination, finite electron lifetime, and diffusion.

According to Ramo's theorem [6], the instantaneous current induced on an electrode by a moving charge q is

$$I = -q \mathbf{v}_{\text{drift}} \cdot \nabla W, \quad (1)$$

where $\mathbf{v}_{\text{drift}}$ is the charge drift velocity, determined by the external electric field and the transport properties of liquid argon, and W is the weighting potential, which is fully defined by the detector geometry. In general, the charge distribution evolves according to coupled partial differential equations describing electrodynamic transport, attachment, and diffusion processes.

For typical LArTPC operating conditions, the transverse and longitudinal diffusion accumulated over meter-scale drift distances remains limited to a few millimeters. Since the induced signal can vary significantly only within a region of a few millimeters near the anode, the evolution of the charge distribution during drift can be factorized from the signal induction process. Diffusion effects are therefore incorporated through a static charge distribution evaluated near the anode plane, while the induced current is computed assuming a unit point charge following the nominal drift trajectory in the vicinity of the electrodes. This factorization substantially simplifies the signal calculation without loss of accuracy.

Under this approximation, the total induced signal $\mathcal{I}(\mathbf{x}_p, t)$ on an electrode located at \mathbf{x}_p is written as

$$\mathcal{I}(\mathbf{x}_p, t) = \int d^2\mathbf{x}' \int dt' i(\mathbf{x}', t'; \mathbf{x}_p, t) q(\mathbf{x}', t'), \quad (2)$$

where $q(\mathbf{x}', t')$ denotes the charge distribution evaluated near the anode, with diffusion effects already incorporated, and $i(\mathbf{x}', t'; \mathbf{x}_p, t)$ is the *field response* function. The field response function, which plays the role of a Green's function for the signal induction problem, is defined by evaluating Eq. (1) for a unit charge drifting along the nominal trajectory, while neglecting attenuation and diffusion effects.

Figure 1 illustrates the full signal formation and processing pipeline. Each track segment in the GEANT4 output is characterized by its endpoints, the total energy loss, and the average energy loss per unit length. These quantities are stored as a single row in a tensor-based representation used

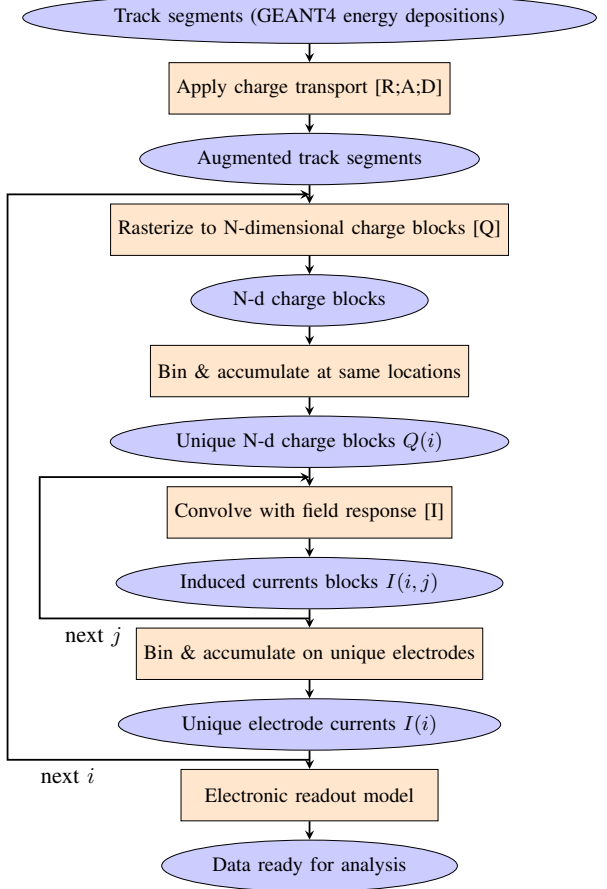


Fig. 1. Flowchart of signal formation and processing from track segments generated in GEANT4 to analysis-ready simulation data. Physics processes are noted in brackets: R: recombination at the initial ionization; A: electron attachment during transport due to finite lifetime; D: drift under the external electric field; Q: rasterization and charge-weighting using Gaussian quadrature rules; I: induced current calculation using the field response function. The side arrows represent the control flow, annotating the outer loop over raster index i and the inner loop over response index j .

by the simulation framework. Based on this initial track-segment representation, detector transport effects are applied to determine the number of ionization electrons that survive recombination and attachment, as well as the characteristic diffusion width accumulated during drift. These quantities are appended to the corresponding tensor row, yielding an augmented track-segment representation. Track segments are then mapped into the N -dimensional domain of the field response sampling, as described in Sec. II-C. For pixelized detectors, $N = 3$: two transverse spatial dimensions and one temporal dimension along the drift paths. This representation is chunked into N -dimensional tensors and the combination of one chunk and the N -dimensional location of its lower corner is called a “block”. Blocks corresponding to identical spatial and temporal coordinates are summed to produce unique N -dimensional blocks. The detector response is subsequently incorporated by convolving these blocks with the field response function, yielding induced currents on the readout electrodes. All contributions are summed to produce a total induced current waveform for each electrode. An electronic readout model is applied to produce signals suitable for higher-level

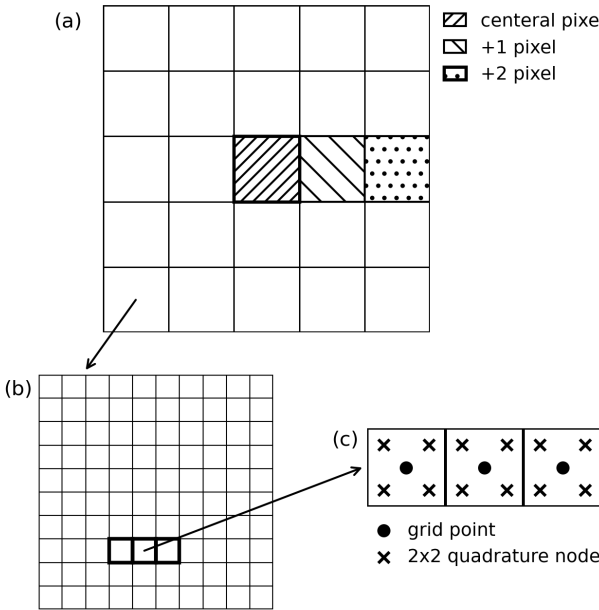


Fig. 2. Illustration of the field response grid and quadrature nodes. (a) Field-response grid defined in pixel pitches, showing the central pixel of interest together with its neighboring pixel areas used in the response calculation. (b) Enlargement of a single pixel area from (a), subdivided into a 10×10 grid of sub-cells, where electrons are released at the center of each sub-cell. (c) Sampling within selected sub-cells, showing the electron release point (dot) and the associated quadrature nodes (crosses) used for the discrete formulation of the detector response in this article.

physics analysis.

B. Induced current modeling

The LArTPC anode is composed of multiple electrodes, whose geometry and arrangement differ between detector designs. Owing to the translational symmetry of the electrode structure, it is sufficient to evaluate the response at a p -th pixel, and to derive the field response at $(p + m)$ -th pixel by $i(\mathbf{x}'; \mathbf{x}_{p+m}) \equiv i(\mathbf{x}'; \mathbf{x}_p + m\mathbf{a}) = i(\mathbf{x}' - m\mathbf{a}; \mathbf{x}_p)$, where $m\mathbf{a}$ is the relative displacement vector from the $p + m$ -th pixel to the p -th pixel. We use $i(\mathbf{r}')$ for the standard field response, when the central electrode is at the origin of the coordinate, and therefore the field response at \mathbf{x}_p can be expressed by $i(\mathbf{x}'; \mathbf{x}_p) = i(\mathbf{x}' - \mathbf{x}_p)$, where $\mathbf{x}' = \mathbf{r}' + \mathbf{x}_p$. Along the drift path, the longitudinal coordinate z is in one-to-one correspondence with time t . The trajectory is integrated using a Runge–Kutta scheme, so that the time points corresponding to nominally constant time steps are obtained approximately. Therefore, the three-dimensional source distribution can be represented as $q(\mathbf{r}' + \mathbf{x}_p, t; t_0)$, and the field response written accordingly as $i(\mathbf{r}', t - t_0)$, where $\mathbf{r}' = (x', y')$ denotes the coordinates within the pixel plane. Equation (2) can be written as

$$\mathcal{I}_p(t) \equiv \mathcal{I}(\mathbf{x}_p, t) = \int d^2\mathbf{r}' \int dt' i(\mathbf{r}', t - t') q(\mathbf{r}' + \mathbf{x}_p, t'), \quad (3)$$

where the electron is located at \mathbf{r}' relative to the fixed electrodes.

In practice, the field-response function $i(\mathbf{r}')$ is computed by fixing the electrode geometry and evaluating the induced

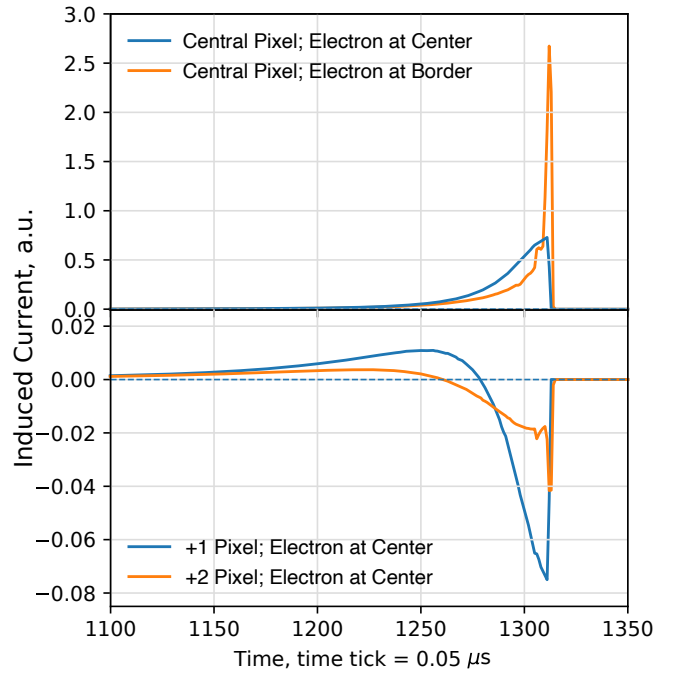


Fig. 3. Induced current from a single drifting electron on the pixelated anode plane of the DUNE ND-LAr detector. Top: response measured on the central (reference) pixel for an electron located at the pixel center and at the pixel boundary. Bottom: responses measured on the first (+1) and second (+2) neighboring pixels for an electron located at the center of the reference pixel. The field response model is generated using COMSOL and validated with the *pochoir* package.

current on a central electrode of interest for charges at different relative positions. Since the induced signal depends only on the relative geometry between the charge and electrodes, this is equivalent to translating the electrodes past a fixed charge, but is simpler and more efficient. Figure 2(b) illustrates the sampling of a single pixel using 10×10 impact partition. Each impact position is located at the center of a partitioned area within the pixel and defines the starting location of a drift path over which the detector response is sampled. Figure 2(c) shows the subsampling scheme within selected impact positions, where the grid point (dot) indicates the electron impact location used for sampling, and the associated quadrature nodes (crosses) are shown for completeness; their definition and role are discussed in Sec. II-C.

Figure 3 shows an example of currents induced by a single electron drifting along selected paths above selected pixels of the DUNE ND-LAr pixelated anode: the top panel compares the center of the collection pixel and a path near the border of the pixel, while the bottom panel shows the +1 and +2 neighboring pixels; the model was produced and validated with COMSOL and *pochoir* packages [7].

C. Effective charge in the simulation

In this section, we discretize the continuous induced current in Eq. (3) using an effective grid-based formulation that preserves fine spatial locality without resorting to dense sampling.

The resulting integrals are evaluated using *Gauss-Legendre quadrature rule*, i.e.,

$$\int_{-1}^1 dx h(x) \approx \sum_i w_i h(\xi_i),$$

where $\{\xi_i, w_i\}$ are the nodes and weights of the N -point Gauss-Legendre rule [8]. In practice, the field response function is evaluated on an equally spaced grid G . We therefore express the induced current as a discrete summation over grid points by introducing an effective charge Q^{eff} on the grid,

$$\mathcal{I}(\mathbf{x}_p, t) = \sum_{g \in G} Q^{\text{eff}}(\mathbf{r}_g, t_g) I(\mathbf{r}_g, t_g; \mathbf{x}_p, t), \quad (4)$$

where $I(\mathbf{r}_g; \mathbf{x}_p) = i(\mathbf{r}_g - \mathbf{x}_p)$ is the field response evaluated at the grid point \mathbf{r}_g in the pixel plane and at the corresponding drift time t_g . This formulation enables Gaussian quadrature on a regular grid, even when the quadrature nodes are not aligned with the grid points. For notational simplicity, the explicit time dependence is suppressed in the following.

We now derive the effective charge by partitioning the detector volume into cuboidal elements whose dimensions match the granularity of the field response function, establishing a one-to-one correspondence with the grid G . The continuous integral can then be written as

$$\int d\mathbf{r}' Q(\mathbf{r}') I(\mathbf{r}'; \mathbf{x}_p) = \sum_C \int_C d\mathbf{r}'_C Q(\mathbf{r}'_C) I(\mathbf{r}'_C; \mathbf{x}_p). \quad (5)$$

where the sum runs over all cuboids C . Applying Gaussian quadrature locally within each cuboid yields

$$\int_C Q(\mathbf{r}') I(\mathbf{r}') d\mathbf{r}' \approx \sum_{l,m,n} w_{lmn} Q_{C,lmn} I_{C,lmn}, \quad (6)$$

where indices (l, m, n) denote the quadrature nodes inside cuboid C .

To evaluate the field response at a quadrature node, we interpolate from the field response function evaluated at nearby grid points. For a quadrature node within a cuboid C , the field response is obtained by trilinear interpolation using the response at the center of C and its twenty-six neighboring cuboids,

$$I_{C,lmn} = \sum_{r,s,t} I_{C,rst} u_{lmn,rst}, \quad (7)$$

where $(r, s, t) \in \{-1, 0, 1\}^3$ denote the cuboid itself (0) and its lower (-1) and upper (1) neighboring cuboids along each axis, and $u_{lmn,rst}$ are the piecewise trilinear interpolation coefficients determined by the relative position of the quadrature node within the cuboid.

Substituting Eqs. (6) and (7) into Eq. (5) yields

$$\begin{aligned} \mathcal{I}(\mathbf{x}_p) &= \sum_C \sum_{l,m,n} w_{lmn} Q_{C,lmn} \left(\sum_{r,s,t} I_{C,rst} u_{lmn,rst} \right) \\ &= \sum_C \sum_{r,s,t} I_{C,rst} \left(\sum_{l,m,n} Q_{C,lmn} w_{lmn} u_{lmn,rst} \right). \end{aligned}$$

Each cuboid C is labeled by indices (i, j, k) along each axis. Together with its neighbors, it spans the set $(i+r, j+s, k+t)$

with $(r, s, t) \in \{-1, 0, 1\}^3$. Combining the summations over cuboids and their neighbors allows Eq. (II-C) to be recast in terms of grid points (i, j, k) ,

$$\mathcal{I}(\mathbf{x}_p) = \sum_{i,j,k} Q_{ijk}^{\text{eff}} I_{ijk}, \quad (8)$$

where the effective charge is defined as

$$Q_{ijk}^{\text{eff}} = \sum_{l,m,n} \sum_{r,s,t} w_{lmn} Q_{lmn,i-r,j-s,k-t} u_{lmn,rst}. \quad (9)$$

The effective charge Q_{ijk}^{eff} thus corresponds to a discrete convolution of the ionization charge at quadrature nodes (l, m, n, i, j, k) with the trilinear interpolation coefficients $u_{lmn,rst}$ along the last three indices.

1) *Calculation of Q for a line-shape track segment*: An ionized track is represented by a series of line segments defined by their two endpoints:

$$\mathbf{p}_0 = (x_0, y_0, z_0) \quad \text{and} \quad \mathbf{p}_1 = (x_1, y_1, z_1).$$

Diffusion is characterized by the coefficients $\sigma_x, \sigma_y, \sigma_z$ in the x, y , and z directions, respectively. The resulting ionization charge distribution is given by the convolution of a uniform line charge with a three-dimensional Gaussian diffusion kernel, and it admits a closed-form expression.:

$$q(x, y, z) = Q \frac{\exp(-B/\Delta^2)}{4\pi\Delta} \times \left(\text{erf}\left(\frac{A_2}{\sqrt{2}\Delta\sigma_x\sigma_y\sigma_z}\right) - \text{erf}\left(\frac{A_1}{\sqrt{2}\Delta\sigma_x\sigma_y\sigma_z}\right) \right) \quad (10)$$

where

$$\begin{aligned} \Delta^2 &= \sigma_y^2 \sigma_z^2 (x_0 - x_1)^2 + \sigma_z^2 \sigma_x^2 (y_0 - y_1)^2 + \sigma_x^2 \sigma_y^2 (z_0 - z_1)^2, \\ A_1 &= \sigma_y^2 \sigma_z^2 (x - x_0)(x_0 - x_1) + \sigma_z^2 \sigma_x^2 (y - y_0)(y_0 - y_1) \\ &\quad + \sigma_x^2 \sigma_y^2 (z - z_0)(z_0 - z_1), \\ A_2 &= \sigma_y^2 \sigma_z^2 (x - x_1)(x_0 - x_1) + \sigma_z^2 \sigma_x^2 (y - y_1)(y_0 - y_1) \\ &\quad + \sigma_x^2 \sigma_y^2 (z - z_1)(z_0 - z_1), \\ B &= \sigma_y^2 (x(z_0 - z_1) + (z_1 x_0 - z_0 x_1) - z(x_0 - x_1))^2 \\ &\quad + \sigma_z^2 (y(x_0 - x_1) + (x_1 y_0 - x_0 y_1) - x(y_0 - y_1))^2 \\ &\quad + \sigma_x^2 (y(z_0 - z_1) + (z_1 y_0 - z_0 y_1) - z(y_0 - y_1))^2, \end{aligned}$$

$\text{erf} :=$ error function.

Accordingly, the discrete charge contribution at the quadrature node (l, m, n) within grid cell (i, j, k) can be written as

$$Q_{lmn,ijk} = q(x_{li}, y_{mj}, z_{nk}).$$

2) *Calculations of Q for short track segments*: In the short-segment limit, Eq. (10) reduces to a point-like Gaussian distribution centered at the segment midpoint. Since the factor Δ appears in the denominator of Eq. (10), this limit can lead to numerical instabilities. To ensure numerical stability, we switch between the point-like and line-shaped formulations: if all components of $\mathbf{p}_1 - \mathbf{p}_2$ are smaller than 0.1σ (configurable) along the corresponding axes, the point-like formulation is used; otherwise, the line-shaped formulation is applied.

D. Interlaced convolution in calculating induced signals

It is useful to rewrite Eqs (3) and (4) as

$$\mathcal{I}_p(\mathbf{x}_p, t) = \sum_{g \in G} Q^{\text{eff}}(\mathbf{r}_g + \mathbf{x}_p, t_g) i(\mathbf{r}_g, t - t_g),$$

which is a cross-correlation in the pixel plane and a convolution along the time direction.

The pixel index p corresponds to a coarser spatial grid with spacing \mathbf{a} than the finer grid G . The finer grid arises from sampling multiple electron impact positions within a single pixel when evaluating the field response function, and thus these impact positions are naturally part of the grid G . Consequently, the set of pixel indices p forms a subset of the grid indices g in the spatial domain; equivalently, the pixel grid can be viewed as a supergrid of G .

We further decompose the grid index into a pair (j, k) , where k labels the pixel and j indexes the sub-pixel grid points, corresponding to the offset λ_j within that pixel. Writing $\mathbf{r}' = \lambda_j + k\mathbf{a}$, we obtain

$$\begin{aligned} \mathcal{I}_p &= \sum_j \sum_k Q^{\text{eff}}(\lambda_j + k\mathbf{a} + \mathbf{x}_p) i(\lambda_j + k\mathbf{a}) \\ &\equiv \sum_j \sum_k Q^{\text{eff}}[j, p + k] i[j, k], \end{aligned} \quad (11)$$

after suppressing the explicit time dependence.

We require the field-response calculation to be symmetric with respect to the central pixel of interest in order to define $R[j, k] \equiv i[j, -k]$, which allows the expression

$$\mathcal{I}_p = \sum_j \sum_k Q^{\text{eff}}[j, p - k] R[j, k]. \quad (12)$$

in which all dimensions appear in a convolution-like structure. We refer to the special treatment in Eq. (12) as an *interlaced convolution*. It should be noted that the effective charge in Eq. (8) is transformed from the grid G to a representation in terms of the pixel grid and its sub-pixel offsets in Eq. (12).

Finally, we note that within the discrete formalism the grid points g need not be uniformly spaced. Any set of grid points may be employed, provided they can be mapped to integer indices. This can be useful to more finely sample the field response in regions near pixel borders where it varies more than pixel centers. Variations in grid spacing are naturally absorbed into the quadrature weights w . In this sense, the discrete convolution introduced here constitutes a generalized numerical formulation.

E. Readout electronics response

There are two liquid argon in-situ charge readout electrode implementations: projective readout and pixelated readout. Each implementation has ramifications for electronics readout system architecture design resulting in tradeoffs for signal extraction fidelity. Both are supported by our simulation framework, and this work focuses on pixelated readout.

Projective readout is implemented as multiple offset planes of arrays of parallel wire or strip electrodes at different angles, providing redundancy for charge reconstruction. Plane offset and wire/strip pitch are at the $\mathcal{O}(1)$ mm-scale. Anode co-planar

coordinates are determined via tomographic projections on all sense planes [9]. Projective readout is typically operated in a manner wherein current waveforms are continuously digitized at a fixed $\mathcal{O}(1)$ MHz sampling rate until a trigger initiates the readout of a portion of waveforms spanning a pre-configured duration. The heat from electronics is well controlled given the moderate number of channels inherent to the projective architecture. The waveform on a channel is a superposition of the induced signal from drifting charges, shaped by the cryogenic preamplifier, front-end filters, and various forms of noise. Several $\mathcal{O}(10^4)$ -channel LArTPC detectors have operated with the projective readout approach [10]–[13].

Pixelated readout is implemented as two dimensional arrays of conductive pixel pads with $\mathcal{O}(1)$ mm pixel pitch on large-format printed circuit boards. Each pixel collects ionization electrons into a uniquely addressable readout channel, enabling native three-dimensional imaging. Each readout channel is an independent self-triggering signal processor capable of amplification, digitization, and multiplexed readout, where $\mathcal{O}(10)$ channels are digitally controlled and configured with an application-specific integrated circuit (ASIC) digital core. Freed ionization electron sparsity permits pixelated readout to nominally operate in a quiescent mode, limiting power dissipation and enabling scaling to $\mathcal{O}(10^7)$ channel systems [2].

In the trigger-reset scheme [14], a digital record encodes the triggered channel's timestamp and an ADC data word, where the latter corresponds to the channel integrated charge at the time of threshold crossing plus a configurable fixed integration duration and the former marks time of digitization with a $\mathcal{O}(10)$ MHz clock. After the triggered readout, the channel is reset and briefly inactive. An example of the trigger-reset readout sequence is shown in Fig. II-E. This design is assumed throughout the rest of the work. A variant trigger logic mode allows multiple, successive digitizations to occur that avoid intervening channel resets [15], mimicking a continuously sampled readout for a fixed duration to evade charge loss at channel reset. In the fixed-charge integration scheme [16], timestamps of integrated fixed charge quanta are recorded and the front-end charge is replenished without charge loss after each trigger. Both schemes operate at the $\mathcal{O}(1)$ kiloelectron channel threshold scale. Charge bias and inefficiencies are incurred from charge left on a channel analog front end due to threshold-based triggering.

III. SOFTWARE DESIGN

A. Array-Oriented, Graph-Based Architecture

Modern GPU architectures are optimized for data-parallel workloads operating on contiguous memory layouts. Accordingly, we adopt an array-oriented design in which the primary data structure is an N -dimensional tensor. Core operations, such as Hadamard (element-wise) products and convolutions, are expressed in idiomatic array form and executed using highly optimized backend libraries. This design aligns naturally with established scientific computing frameworks, and

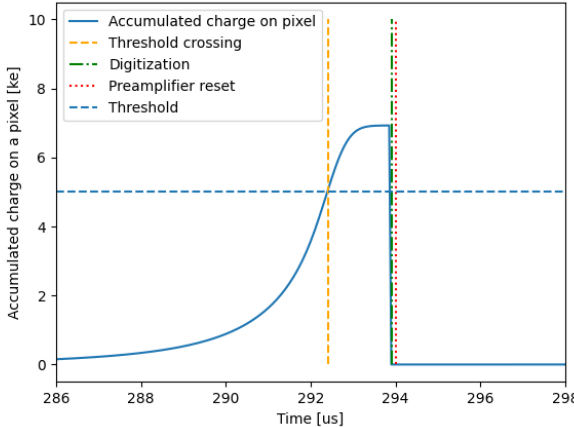


Fig. 4. Trigger-reset scheme of the LArPix ASIC [14]. Two consecutive hits are illustrated. The channel threshold is represented by a horizontal dashed line. The vertical dashed line indicates the time at which the input signal crosses the discriminator threshold. The integrated charge on the preamplifier is sampled after a fixed window, marked by the dash-dotted line. Following a short reset interval, ending at the dotted line, charge accumulation on the preamplifier resumes.

we use PyTorch is used as the backend due to its mature GPU support and extensive user community.

To structure the computation, we adopt a graph-based architecture in which each operation is encapsulated as a PyTorch `nn.Module` (a graph-node) with well-defined inputs and outputs. These modules form a directed acyclic graph that mirrors the simulation pipeline, shown in Fig. 1. By packaging computational kernels as modules, we delegate kernel dispatch, device and stream placement, and memory management to the PyTorch runtime, while naturally enabling practical capabilities such as automatic batching, mixed precision, and profiler-guided optimization. The module abstraction provides a uniform interface that substantially improves composability, testability, and long-term maintainability.

1) *Effective charge calculation*: The expression for Q_{ijk}^{eff} from Eq. (9) can be interpreted as an element-wise product with quadrature weights, followed by convolution with trilinear coefficients. The quadrature weights are mapped from the standard interval $[-1, 1]$ to the local intervals surrounding each grid point. The trilinear coefficients u depend only on the quadrature node positions within the standard interval, and therefore, can be precomputed. The resulting formulation closely resembles a three-dimensional convolution (Conv3D) with a small-support kernel u , enabling particularly efficient evaluation on GPU architectures.

2) *Mirror-Pair Complex Packing (MPCP) Convolution*: As noted in Sec. II-A, the induced current on the electrodes arises from the convolution between the effective charge distribution and the field response function. This is realized by partitioning the entire space into sub-grids according to the impact positions of electrons relative to the electrode centers. In machine learning terminology, this corresponds to a channel-wise convolution followed by a summation over channels. Partitioning the input prior to convolution is equivalent to

array slicing in array-oriented languages. To accelerate the computation with a large kernel (the field response), we employed an FFT-based linear convolution technique. It is also important to note that the field response exhibits reflection symmetry with respect to the electrode's center. We employ a method, named “Mirror-Pair Complex Packing (MPCP)”, to further boost the calculation.

To illustrate this, consider an one-dimensional case. For each sub-electrode offset j , the response observed at the i -th electrode is denoted as R_i^j . The induced current at electrode position p is then given by

$$I_p = \sum_{i,j} Q_i^j R_{p-i}^j,$$

where each charge element Q_i^j contributes according to the offset $p - i$ from its position. Under reflection symmetry, the response satisfies

$$R_{-i}^j \equiv R_i^j.$$

Using this condition, the induced current can be written as

$$\begin{aligned} I_p &= \sum_{j=-N, j \neq 0}^N \sum_i R_i^j Q_{p-i}^j \\ &= \sum_{j=1}^N \sum_i R_i^j (Q_{p-i}^j + Q_{p+i}^{-j}) \\ &= \sum_{j=1}^N \sum_i R_i^j (Q_{p-i}^j + Q_{-(p'-i)}^j), \end{aligned} \quad (13)$$

where $p' = -p$. The second term corresponds to a reflection in both the input index and the output position.

Although the ionization terms do not combine into a single convolution because of the absence of reflection symmetry in the ionization charge, the two contributions can still be evaluated efficiently. Note that the pair of channels can be packed into a single complex array, $Q^j + i Q^{-j}$ (with $i^2 = -1$), so they are transformed simultaneously and do not interfere during the FFT operations. This complex packing reduces the number of FFTs.

It is worth noting that the multi-channel convolution can be evaluated efficiently in the frequency domain:

$$\begin{aligned} I_p &= \sum_j \text{IFFT}(\text{FFT}(R^j) \text{FFT}(Q^j)) \\ &= \text{IFFT} \left(\sum_j \text{FFT}(R^j) \text{FFT}(Q^j) \right). \end{aligned} \quad (14)$$

Consequently, with precomputed $\text{FFT}(R^j)$, each evaluation requires one forward FFT per (packed) impact position and a single global inverse FFT; MPCP further halves the number of forward FFTs.

B. Resources management

1) *Block sparse binned tensor*: A LArTPC with pixelated readout comprises thousands of readout channels and a large number of time samples along the drift direction. At the same time, neutrino interactions produce ionization signals that are

highly localized in both space and time. The combination of a large detector readout space and intrinsically sparse signal activity makes it impractical and computationally inefficient to track the induced current on every pixel at every time sample. An efficient representation therefore requires the use of sparse data structures.

We exploit sparsity by implementing a concept called block-sparse binned tensor. In this scheme, dense data are stored within blocks, where each block is composed of an N -dimensional array and an accompanying length- N vector. The array stores the physical values at grid points, while the vector specifies the coordinates of the block's lower corner. Blocks have a regular shape and can be batched for GPU processing. The entire detector volume (or a sub-volume of interest) is partitioned into such bins, but only those containing event activity are retained. Importantly, bin positions are required to align with the bin boundaries of the enclosing volume.

Beyond storage efficiency, the block-sparse binned tensor provides additional functionalities for simulation. First, it allows input arrays to be aligned and cropped to bin boundaries. Second, it handles cases where diffusion and convolution of field response function enlarge the data footprint, causing originally disjoint inputs to produce overlapping outputs. This overlap can create contention during subsequent parallel operations. The block-sparse binned tensor resolves this issue by reducing overlapping regions (using summation or other reduction operations) implemented efficiently through PyTorch's `scatter_add` backend. The concept of the block-sparse binned tensor is analogous to the histogram described in Ref. [17]. However, in this work, all data are organized and processed in binned blocks, requiring additional mapping and reduction operations between high-dimensional tensors, rather than simple scalar additions.

2) *Batching and chunking for sparse data:* Fixed batch sizes are commonly used in traditional workflows, but they are poorly suited to sparse signals: localized bursts of activity can produce transient peaks in memory usage that undermine predictable resource control. To address this, we replace globally fixed batching and batch-only chunking with two complementary strategies. Hierarchical batching dynamically adjusts the batch size to the realized sparsity and computational load, while sub-dimensional chunking partitions tensors along orthogonal spatial or temporal axes, such as the electron drift direction, to bound memory consumption without sacrificing throughput. As an example, during rasterization of GEANT4 track segments onto a spatial grid (described in Sec. II-A), different segments intersect different numbers of grid cells, resulting in a variable number of rasterized blocks even for fixed-size inputs. To accommodate this variability while maintaining efficient downstream execution, we perform a re-batching step that reorganizes the rasterized blocks into batches of appropriate size. This re-batching groups blocks according to their realized occupancy and workload, ensuring balanced computation and bounded memory usage in subsequent processing stages.

Hierarchical batching also applies in cases where downstream operations increase tensor dimensionality and require additive reductions. In LArTPC simulations, both rasterization

and field-response convolution expand the spatial support of the signal, leading to overlapping contributions that must be accumulated before subsequent processing steps. Because these reductions are linear, the ordering of batching operations does not affect the final result to a noticeable level.

Furthermore, evaluating the effective charge using quadrature introduces additional node axes along each dimension, increasing the data volume multiplicatively with the number of quadrature nodes. As a result, even modest batch sizes can become memory intensive. To control memory usage, we partition the computation by chunking tensors along orthogonal axes, such as the electron drift direction. Each chunk is processed independently and sequentially, bounding peak memory consumption while preserving overall throughput.

A summary of control flow is illustrated in Fig. 1. The augmented features from the global batched input are divided into smaller batches i during the rasterization process. Each rasterized batch is then further split into sub-batches j , which are processed through convolution. The resulting outputs are binned and accumulated, as described in Sec. III-B1, to obtain the induced current at unique pixel locations for each (i, j) pair. For each rasterized batch i , the currents are summed over the unique pixels. After iterating over all i -batches, a final concatenation and accumulation step is performed to combine the contributions from the entire global input.

IV. PERFORMANCE EVALUATION

A. Test data and simulation setup

The data sample used in this study corresponds to the anti-neutrino beam configuration at the DUNE-ND site. The neutrino-argon interaction cross section in the LArTPC are simulated using the GENIE event generator [18]. On average, about $\mathcal{O}(50)$ neutrino interaction vertices occur within ND-LAr for each spill of the primary proton beam.. The GENIE outputs are then passed to `edep-sim` [19], [20], a GEANT4-based simulation framework, to estimate the energy depositions from the products of neutrino-argon interactions inside the detector. The ND-LAr detector consists of 7×5 TPC modules, each comprising two drift volumes separated by a central cathode. Each drift volume has a maximum drift length of approximately 50 cm and is instrumented with a pixelated anode plane. Each anode plane is approximately 1 m long in the neutrino beam direction and 3 m tall. Figure 5 shows the distribution of input track segments per neutrino beam spill and per TPC drift volume, simulated with GEANT4. We initially focus on cases with fewer than $\mathcal{O}(5000)$ track segments; as demonstrated later, the performance of our approach scales readily to larger occupancies.

The field response is calculated on a 5×5 pixel grid, and spanning approximately 15 cm along the nominal drift direction, corresponding to about 2000 time ticks at 50 ns per tick. We use a baseline setup where the area around an electrode is divided into 10×10 subregions, to sample the field response function. This resolution captures the relevant spatial features of the response. This choice also aligns with

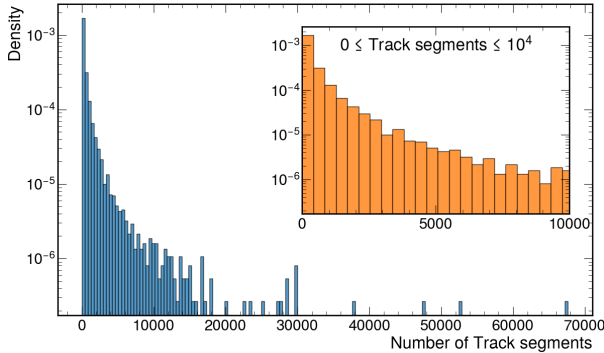


Fig. 5. Distribution of the number of track segments per neutrino beam spill and per TPC drift volume, simulated from `edep-sim`.

the typical diffusion width, which is comparable to or larger than the subgrid spacing in this configuration most of the time. The geometry is illustrated in Fig. 2. The readout model assumes the LArPix detector design, as described in Sec. II-E.

The rasterized charges are grouped into 4×4 pixels and 32 time ticks before convolution. The convolution output is then padded to $8 \times 8 \times 2048$ to maintain high performance by using power-of-two dimensions. The choice of 32 time ticks is motivated by the runtime study shown in Fig. 11. The waveform input to the readout electronics model is configured to span $600\mu\text{s}$ (approximately 96 cm), corresponding to twice the maximum drift length of the DUNE-ND modules. The tests were performed on an NVIDIA GeForce RTX 4090 GPU with 24 GB of memory using 64-bit float numbers.

A neutrino event in a single TPC drift volume from the simulation is given in Fig. 6.

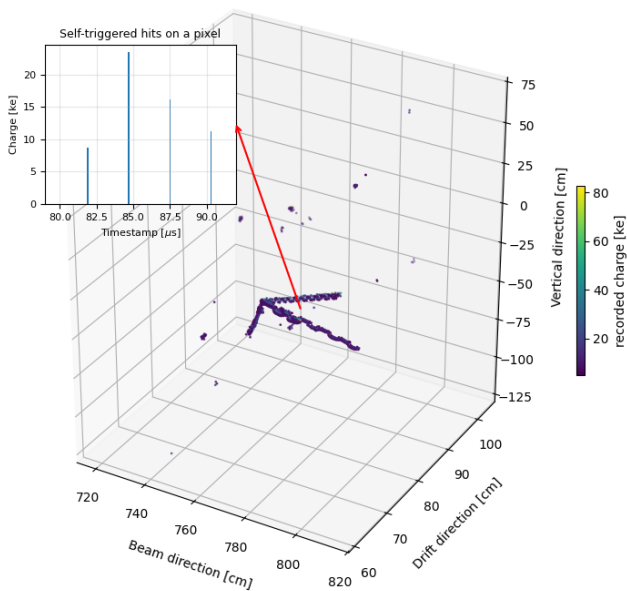


Fig. 6. Event display of a neutrino interaction in a single ND-LAr TPC drift volume.

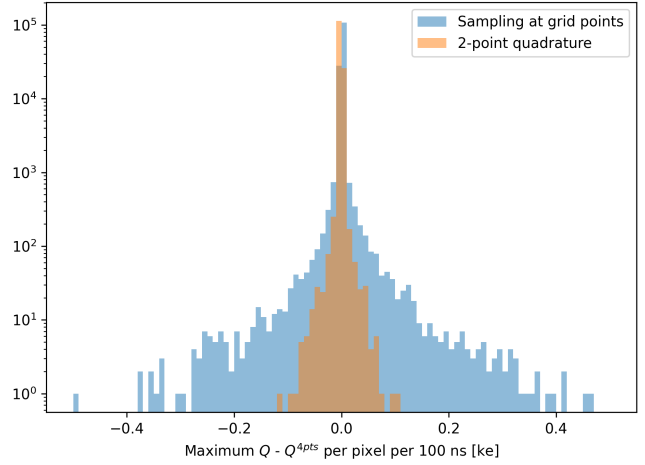


Fig. 7. The maximum deviations of accumulated charge per pixel channel per 100ns, under sampling at grid points, or two-point quadrature rule, relative to the reference charge under 4-point quadrature rule.

B. Performance Benchmarks: Accuracy, GPU Memory Usage, and Runtime

Figure 7 presents the accuracy study. The maximum deviation of the accumulated charge per pixel channel within a 100 ns window is evaluated for normal sampling at grid points and for the two-point quadrature rule, each relative to the reference obtained using the four-point quadrature rule. Taking the higher-order quadrature as a reference, the substantially narrower spread observed for the two-point quadrature, compared to normal sampling, demonstrates that the effective-charge approach captures the fine structure of the induced waveform without requiring a finely gridded field response function. The observed deviations are well below the typical equivalent noise level of front-end electronics in LArTPCs, $\mathcal{O}(500\text{e}^-)$.

One key challenge in the GPU programming lies in managing memory usage. The hierarchical batching and sub-dimensional chunking strategies described in Sec. III-B2 address the data volume increase introduced by applying both the quadrature rule and convolution. The upper panel of Fig. 8 shows the peak GPU memory usage with hierarchical batching enabled and chunking disabled. For a rasterization batch size of $i = 100$, the memory usage increases only gradually with activity, reflecting the slow growth of the output-dominated contribution. As event activity increases, all configurations converge to the same asymptotic memory usage, since the dominant memory footprint is determined by long per-pixel waveforms that are independent of batching or chunking parameters. In contrast, when the rasterization batch size is increased to $i = 300$, a rapid rise in memory usage is observed at low activity, because memory consumption is no longer dominated by the output tensors but instead by intermediate states generated during the rasterization step, including the sparse representations of accumulated charge blocks. These intermediate structures scale strongly with the rasterization batch size and therefore drive the observed memory increase. GPU memory usage can be further reduced by chunking along

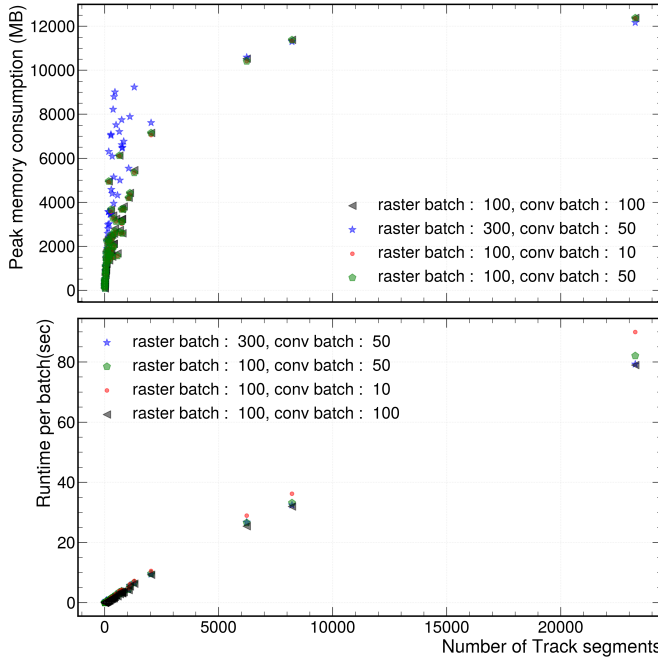


Fig. 8. GPU memory usage (top) and runtime (bottom) per TPC drift volume as a function of the number of input tracks segments for different batching schemes. **Top:** GPU memory usage per batch when the hierarchy batching is enabled, and the hierarchy chunking is disabled. **Bottom:** Runtime per batch when the hierarchy batching and chunking are enabled.

feature dimensions, as described in Sec.III-B2. We evaluate this effect by applying different chunk sizes along a single axis in the pixel plane. As shown in Fig. 9, introducing chunking significantly lowers peak memory consumption compared with the unchunked case, with reductions of approximately a factor of 2–5 depending on the chunk size.

We now examine its impact on runtime performance. The lower panel of Fig. 8 shows the corresponding GPU runtime per batch for different combinations of raster batching (ionization-charge batching) and convolution batching. For a fixed raster batch size, comparing different convolution batch sizes demonstrates that the overhead introduced by splitting the computation into smaller batches is minimal. A noticeable runtime increase of about 10% is observed only when the convolution batch size is reduced to 10. Beyond this point, the runtime scales approximately linearly with input size, indicating that the GPU resources are fully utilized and that performance is dominated by the computational workload rather than batching overhead.

We analyze the runtime performance broken down by operation. One batching scheme is selected since the differences among schemes are minor. Figure 10 shows the runtime distribution among the major operations aggregated across all TPCs. The large slice for the convolution indicates that the convolution dominates the overall execution time and constitutes the principal performance bottleneck. The block-sparse binning of the charge blocks is the second most time-consuming operation.

We further evaluate the runtime performance for different choices of bin size in the block-sparse binned tensor representation. Figure 11 shows the GPU runtime of the

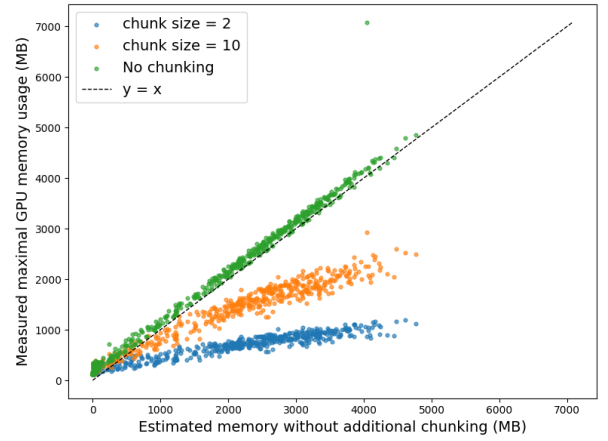


Fig. 9. Memory usage with chunking over one axis in the pixel plane, shown as a function of the estimated memory usage without chunking over the feature dimensions. The dashed line indicates the ideal case where the measured memory usage coincides with the estimated value. Green points indicate the memory usage without chunking over the feature dimensions. Blue and orange points show the results for chunk sizes of 2 and 10, respectively.

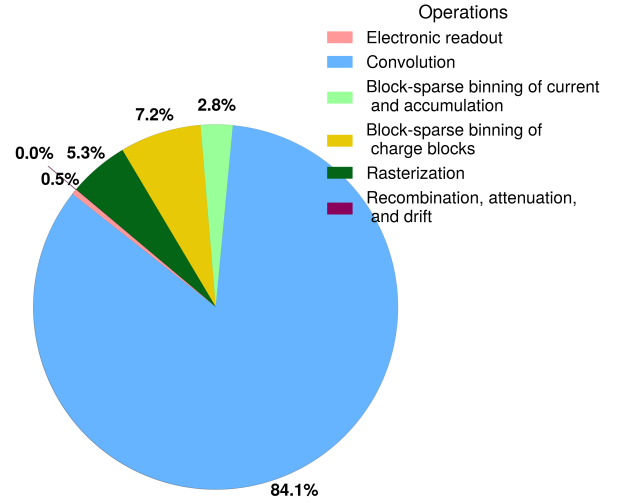


Fig. 10. Runtime share among the major operations on the GPU. Each slice represents an operation's total runtime relative to the total execution time.

block-sparse binning operation applied to the charge blocks as a function of the bin size along the time axis. As the bin size increases, the runtime also increases. This behavior arises because larger bins tend to include a higher fraction of zero entries, reducing the effectiveness of sparsity and increasing unnecessary computation. In the temporal direction, the typical extent of ionization-charge segments ranges from approximately 50 to 150 ticks. For bin sizes below about 50 ticks, the runtime remains both fast and stable, indicating that sparsity is effectively preserved in this regime. As the bin size increases beyond this scale, the performance degrades as bins increasingly encompass regions without signal.

These observations indicate that optimal performance is achieved by choosing a bin size smaller than the characteristic

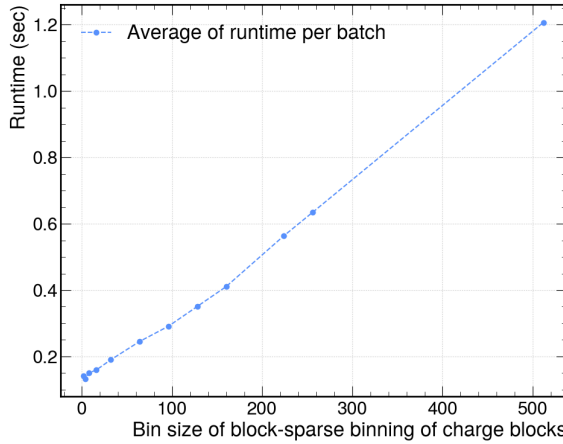


Fig. 11. Runtime for converting blocks into a block-sparse binning representation as a function of bin size. Each point shows the average time for the block-sparse binning operation applied to the same charge blocks.

size of the input charge blocks. However, this choice involves a trade-off, since the block-sparse binned tensor serves as the input to subsequent operations. For example, when used as input to a convolution, bins that are much smaller than the field response increase the number of convolution operations, while the output size changes only marginally. As a result, excessively small bin sizes can lead to increased overall runtime despite faster binning. An optimal bin size therefore balances efficient sparse binning against the computational cost of downstream operations.

V. DISCUSSIONS

We have presented the performance of the TRED package and demonstrated that its analytical treatment of effective charge enables accurate and efficient induced-current calculations. In this section, we discuss key aspects of the effective-charge formulation and software architecture, examine its suitability for calibration and differentiable simulation workflows, and outline potential extensions of the approach to other detector configurations, including the DUNE far detector.

A. Accuracy, Applicability, and Numerical Considerations of Charge Calculation

The accuracy of the quadrature-based formulation depends on the relative scale of the integration intervals and the diffusion width of the charge distribution. When the grid spacing is significantly larger than the diffusion width, the approximation degrades, as the charge distribution is insufficiently resolved. In practice, this situation may arise either when diffusion is negligibly small or when the simulation grid is chosen too coarsely. The former is uncommon in large liquid-argon TPCs and similar neutrino detectors, where long drift distances naturally lead to substantial diffusion, and can be further mitigated by imposing a minimum diffusion scale in the simulation. The latter can be readily avoided by selecting a grid spacing commensurate with the expected diffusion scale, a choice that remains under user control.

More generally, many simulation frameworks for projective readout detectors treat individual energy depositions as point-like objects prior to diffusion. The effective-charge formalism introduced here remains applicable in such cases, provided a suitable criterion is adopted to transition between point-like and extended (line-like) representations. This flexibility allows the method to be used consistently across different detector models and simulation paradigms.

We also note that mapping interpolation coefficients from the field response to the charge density at quadrature nodes can introduce mild smearing near pixel boundaries. This arises because the transition from unipolar signals in the central collection pixel to bipolar currents in neighboring pixels occurs over a very short spatial scale. Interpolation across this sharp transition can smooth the response and lead to a small spreading of charge across pixel boundaries. In practice, this effect is confined to a narrow region near pixel edges and becomes negligible when the grid spacing is sufficiently fine, as the fraction of affected grid points scales with the boundary area rather than the pixel volume. Moreover, the smearing can be corrected if needed by applying boundary-aware interpolation or post-processing corrections. In our tests, the effect is already strongly suppressed due to the use of fine spatial grids and continuous charge distributions, and any residual impact is negligible, shown in Fig. 7.

B. Software Abstractions and Broader Applicability

The package presented in this work emphasizes abstraction and deliberately leverages concepts and tools from the broader computational science community—particularly those developed for machine learning to enhance long-term maintainability and extensibility. This design choice also provides a potential pathway toward portability across diverse hardware architectures supported by PyTorch backends, as these ecosystems continue to mature. The extent to which such portability can be realized while maintaining competitive performance remains an important subject for future investigation.

The block-sparse binned tensor introduced here further serves as an effective abstraction for computational problems that require careful coordination of concurrent memory reads and writes, such as those encountered in sparse neural network implementations. Many existing frameworks either provide limited support for these access patterns or are restricted to two-dimensional sparse tensors. For example, `SparseConvNet` and `MinkowskiEngine` represent multi-dimensional sparsity using coordinate (COO) formats, which are not well suited for FFT-based operations. In contrast, the block-sparse binned tensor formulation naturally supports structured sparsity in higher dimensions while remaining compatible with convolutional and FFT-based workflows.

C. Differentiable Simulation and Calibration Potential

The PyTorch-based implementation also enables end-to-end simulation and optimization by directly comparing simulated outputs with data from calibration sources [21]. Unlike traditional calibration workflows in particle physics, which typically adjust parameters sequentially and in isolation, an

end-to-end approach allows all relevant parameters to be optimized simultaneously within a unified framework. This can improve internal consistency between simulation components and enhance the efficiency and accuracy of detector modeling.

Within our framework, the input parameters of individual computational layers can, in principle, be optimized automatically using the output data, forming a differentiable and self-consistent calibration pipeline. As a proof of concept, we demonstrate the tuning of the electron lifetime by assuming access to simulated waveforms, corresponding reference (“true”) waveforms, and source information for test samples. The results are shown in Fig. 12. The true electron lifetime is set to 0.8 ms, and two initial values are chosen to be 1.2 and 0.8 times the true value. Using the same input source, the electron lifetime is optimized through differentiable simulation over many epochs, converging toward the true value regardless of the initial condition.

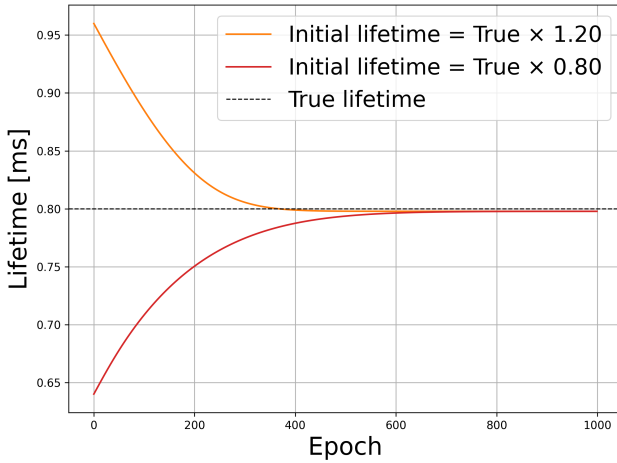


Fig. 12. Electron lifetime as a function of training epoch (iteration). The dashed line indicates the true lifetime, while the solid lines correspond to different initial values.

We emphasize, however, that automatic calibration is not a core design goal of the framework. Gradient-based optimization requires intermediate states to be retained until the end of each optimization epoch, which limits memory reuse and can significantly increase memory consumption. Moreover, the ground-truth information required for such end-to-end calibration is generally unavailable in real experimental conditions. As a result, while the framework supports differentiable simulation and optimization, its primary focus remains fast and accurate forward simulation rather than automated calibration.

D. Relation to Existing ND Simulation Tools

For the DUNE Near Detector, the existing simulation package `larnd-sim` [3] employs custom GPU kernels with just-in-time compilation via Numba [22], managing data in raw arrays and enforcing sparsity through pixel-level operations. While both frameworks simulate the same underlying detector physics, they differ substantially in software architecture, abstraction level, and use of community-driven ecosystems. A detailed, quantitative comparison of performance, resource

usage, and physics validation between TRED and existing ND simulation frameworks, including comparisons with experimental data, is deferred to future work.

E. Extension to Far-Detector Simulations

The TRED package was developed with a primary focus on the DUNE Near Detector, which employs zero-suppressed front-end electronics. Nevertheless, the underlying functions and tools are readily extendable to continuously sampled readout detectors, such as the DUNE Far Detector, by replacing the field-response-only model with a combined field-response and electronics-response formulation. Because the response functions are precomputed, this extension introduces no additional computational overhead during simulation.

As a proof of concept, test cases in the cosmic-ray environment of the ProtoDUNE Single-Phase detector [23], simulated using `Wire-Cell` [24], demonstrate a speed improvement of approximately a factor of three on CPU architectures. This performance gain highlights the effectiveness of the sparse data representation employed by TRED. In contrast, the standard `Wire-Cell` workflow defines a global region of interest for each drift volume and performs convolution on a dense representation of the signal using a detector response function that combines both field and electronics effects.

The advantages of TRED become even more pronounced for far-detector simulations that require long readout windows. While a beam spill at DUNE spans $\mathcal{O}(3 \text{ ms})$, set by the maximum electron drift time, simulations of supernova neutrino bursts must cover time scales of order 100 s to capture all relevant activity. A supernova within our galaxy ($\sim \mathcal{O}(10) \text{ kpc}$) is expected to produce $\mathcal{O}(10^3)$ detectable neutrino interactions in the DUNE Far Detector [25], making full-window simulation with dense representations computationally challenging. In this regime, the sparse, block-based approach of TRED offers a particularly attractive path toward scalable far-detector signal simulation.

VI. SUMMARY

In summary, we have presented TRED, a GPU-accelerated simulation package that enables accurate and efficient modeling of charge signal formation in liquid argon time projection chambers. The core of the approach is an analytic effective-charge formulation based on Gaussian quadrature, which captures sub-grid structure without requiring dense sampling. In conjunction with this, we introduce a generic block-sparse binned tensor representation that supports efficient reduction operations on sparse signals and enables the direct application of FFT-based algorithms to localized regions of the detector volume. Together, these components yield an FFT-based analytic solution for induced signals that demonstrates strong performance in both runtime and GPU memory usage under beam conditions and pile-up levels expected at DUNE-ND, while remaining applicable to other large-scale detectors with sparse activity, including DUNE-FD.

More broadly, the design principles and data abstractions introduced in TRED extend beyond a single detector or experiment. By combining analytic signal modeling with sparse, block-structured tensor representations and

community-supported GPU software, this work demonstrates a scalable and sustainable approach to detector simulation for experiments characterized by large volumes and highly localized activity. These concepts are readily transferable to other neutrino detectors and to computational domains that require efficient processing of large, sparsely activated datasets.

ACKNOWLEDGEMENT

We thank Matt Kramer, Dan Dwyer, Alex Booth, and Haiwang Yu for their helpful input on existing simulation frameworks. We especially thank Matt Kramer for his thorough review of the manuscript. The work was supported by the U.S. Department of Energy (DOE), Office of Science, Office of High Energy Physics, under Contract No. DE-SC0012704. We also acknowledge the use of ChatGPT for language editing.

REFERENCES

- [1] B. Abi *et al.*, “Deep Underground Neutrino Experiment (DUNE), Far Detector Technical Design Report, Volume I Introduction to DUNE,” *JINST*, vol. 15, no. 08, p. T08008, 2020.
- [2] V. Hewes *et al.*, “Deep Underground Neutrino Experiment (DUNE) Near Detector Conceptual Design Report,” *Instruments*, vol. 5, no. 4, p. 31, 2021.
- [3] A. Abed Abud *et al.*, “Highly-parallelized simulation of a pixelated LArTPC on a GPU,” *JINST*, vol. 18, no. 04, p. P04034, 2023.
- [4] A. Paszke *et al.*, “Pytorch: An imperative style, high-performance deep learning library,” 2019. [Online]. Available: <https://arxiv.org/abs/1912.01703>
- [5] B. Graham *et al.*, “Submanifold sparse convolutional networks,” *arXiv preprint arXiv:1706.01307*, 2017.
- [6] S. Ramo, “Currents induced by electron motion,” *Proceedings of the IRE*, vol. 27, no. 9, p. 584, 1939.
- [7] S. Martynenko *et al.*, “A hybrid 3d/2d field response calculation for liquid argon detectors with pcb based anode plane,” *Journal of Instrumentation*, vol. 18, no. 04, p. P04033, apr 2023. [Online]. Available: <https://doi.org/10.1088/1748-0221/18/04/P04033>
- [8] W. Gautschi, “On the construction of Gaussian quadrature rules from modified moments,” *Mathematics of Computation*, vol. 24, no. 110, p. 245, Apr. 1970. [Online]. Available: <https://doi.org/10.1090/S0025-5718-1970-0285117-6>
- [9] X. Qian *et al.*, “Three-dimensional Imaging for Large LArTPCs,” *JINST*, vol. 13, no. 05, p. P05032, 2018.
- [10] R. Acciarri *et al.*, “Design and Construction of the MicroBooNE Detector,” *JINST*, vol. 12, no. 02, p. P02017, 2017.
- [11] —, “Construction of precision wire readout planes for the Short-Baseline Near Detector (SBND),” *JINST*, vol. 15, no. 06, p. P06033, 2020.
- [12] L. Bagby *et al.*, “Overhaul and Installation of the ICARUS-T600 Liquid Argon TPC Electronics for the FNAL Short Baseline Neutrino Program,” *JINST*, vol. 16, no. 01, p. P01037, 2021.
- [13] A. A. Abud *et al.*, “Design, construction and operation of the ProtoDUNE-SP Liquid Argon TPC,” *JINST*, vol. 17, no. 01, p. P01005, 2022.
- [14] D. A. Dwyer *et al.*, “LArPix: Demonstration of low-power 3D pixelated charge readout for liquid argon time projection chambers,” *JINST*, vol. 13, no. 10, p. P10007, 2018.
- [15] J. Asaadi *et al.*, “Novel Liquid Argon Time-Projection Chamber Readouts,” *Annu. Rev. Nucl. Part. Sci.*, vol. 74, pp. 529–555, 2024.
- [16] D. Nygren *et al.*, “Q-Pix: Pixel-scale Signal Capture for Kiloton Liquid Argon TPC Detectors: Time-to-Charge Waveform Capture, Local Clocks, Dynamic Networks,” 9 2018. [Online]. Available: <https://arxiv.org/abs/1809.10213>
- [17] J. H. Ahn *et al.*, “Scatter-add in data parallel architectures,” in *11th International Symposium on High-Performance Computer Architecture*, 2005, pp. 132–142.
- [18] C. Andreopoulos *et al.*, “The GENIE Neutrino Monte Carlo Generator: Physics and User Manual,” FERMILAB-FN-1004-CD, Tech. Rep., 10 2015.
- [19] C. McGrew *et al.*, “edep-sim: An energy deposition simulation,” <https://github.com/ClarkMcGrew/edep-sim>, GitHub repository.
- [20] S. Agostinelli *et al.*, “GEANT4 - A Simulation Toolkit,” *Nucl. Instrum. Meth. A*, vol. 506, p. 250, 2003.
- [21] S. Gasiorowski *et al.*, “Differentiable simulation of a liquid argon time projection chamber,” *Machine Learning: Science and Technology*, vol. 5, no. 2, p. 025012, apr 2024. [Online]. Available: <https://doi.org/10.1088/2632-2153/ad2cf0>
- [22] S. K. Lam *et al.*, “Numba: A LLVM-based Python JIT Compiler,” in *Proc. Second Workshop on the LLVM Compiler Infrastructure in HPC*, Nov. 2015, p. 1.
- [23] B. Abi *et al.*, “The Single-Phase ProtoDUNE Technical Design Report,” DUNE, Tech. Rep. FERMILAB-DESIGN-2017-02, 6 2017.
- [24] C. Adams *et al.*, “Ionization electron signal processing in single phase LArTPCs. Part I. Algorithm Description and quantitative evaluation with MicroBooNE simulation,” *JINST*, vol. 13, no. 07, p. P07006, 2018.
- [25] B. Abi *et al.*, “Supernova neutrino burst detection with the Deep Underground Neutrino Experiment,” *Eur. Phys. J. C*, vol. 81, p. 423, 2021.